International Journal of Rock Mechanics & Mining Sciences 59 (2013) 57–69

Contents lists available at SciVerse ScienceDirect

International Journal of Rock Mechanics & Mining Sciences

journal homepage: www.elsevier.com/locate/ijrmms

Universal criteria for rock brittleness estimation under triaxial compression

Boris Tarasov [a,*], Yves Potvin [b]

[a] Centre for Offshore Foundation Systems, The University of Western Australia, 35 Stirling Highway, Crawley, Western Australia 6009, Australia
[b] Australian Centre for Geomechanics, The University of Western Australia, 35 Stirling Highway, Crawley, Western Australia 6009, Australia

ARTICLE INFO

Article history:
Received 3 November 2011
Received in revised form
19 September 2012
Accepted 18 December 2012
Available online 18 January 2013

Keywords:
Rock brittleness criteria
Confined compression
Post-peak energy balance
Scale of brittleness
Intrinsic and relative brittleness

ABSTRACT

Brittleness is one of the most important mechanical properties of rock; however, the concept of brittleness in rock mechanics is yet to be precisely defined. Many brittleness criteria have been proposed to characterise material behaviour under compression, but there is no consensus as to which criteria is the most suitable and reliable.

This paper considers brittleness at compression as the rock capability to self-sustaining macroscopic failure in the post-peak region due to elastic energy accumulated within the loaded material. The applicability of various criteria for assessing rock brittleness from this point of view is analysed. It is shown that only two of many existing criteria can describe properly the intrinsic material brittleness within the whole range of brittleness variation from the absolute brittleness to ductility. These criteria rely upon post-peak energy balance and are based on sound physics principles. Unlike other existing criteria they allow for the representation of two classes of rock behaviour (Class I to Class II) in the form of continuous, monotonic and unambiguous scale of brittleness. The effect of confining pressure on rock brittleness is analysed where rock behaviour can be changed from Class I to Class II and then to Class I again.

1. Introduction

Brittleness is a very important mechanical property of intact rock because it has a strong influence on the failure process and on the rock mass response to mining or tunnelling activities. Large seismic events are often produced when rock masses are submitted to triaxial compression generating violent shear failures. The correct determination of brittleness at such loading conditions is important to better predict and mitigate these dynamic events. However, the concept of brittleness in rock mechanics is yet to be precisely defined. Several brittleness criteria have been proposed to characterise material behaviour under compression [1–19], but there is no consensus as to which criteria is the most suitable and reliable. The following approach for brittleness estimation at confined compression ($\sigma_1 > \sigma_2 = \sigma_3$) is used in the paper.

Experiments show that when loading a rock specimen, the specimen deformation is always macroscopically stable and controllable, before the peak stress is reached. Macroscopic instability associated with strength degradation in the form of spontaneous failure can only take place in the post-peak region. The post-peak instability can be treated as a manifestation of rock brittleness. In this paper, the degree of post-peak instability estimated on the basis of post-peak energy balance is used for rock brittleness characterisation at compression.

The degree of post-peak instability caused by solely elastic energy stored within the loaded material is classified as *intrinsic brittleness*, while the degree of post-peak instability in relation to elastic energy accumulated in the loading system is classified as *relative brittleness*. The paper focuses mainly on criteria characterising intrinsic rock brittleness. The concept takes into account the fact that elastic energy distributed quite evenly within the material body at peak stress represents the source of energy for localised post-peak failure in the form of shear rupture typical for confined compression. Features of the post-peak energy balance at the localised failure are discussed.

The paper analyses how different existing brittleness indices reflect the degree of post-peak instability. It is shown that only two of many existing criteria can describe properly the intrinsic material brittleness within the whole range of brittleness variation from the absolute brittleness to ductility. These criteria allow for the representation of two classes of rock behaviour (Class I and Class II) in the form of continuous, monotonic and unambiguous scale of brittleness. This universal scale is used to illustrate some features of brittleness variation as a function of rising confining pressure for different rocks where rock behaviour can be changed from Class I to Class II and then to Class I again.

2. Principles of brittleness estimation on the basis of post-peak energy balance

Informative characteristics of intrinsic material properties, before and after the peak stress is reached, can be obtained from

* Corresponding author. Tel.: +61 8 9380 7368; fax: +61 8 9380 1044.
E-mail address: tarasov@civil.uwa.edu.au (B. Tarasov).

1365-1609/$ - see front matter © 2013 Elsevier Ltd. All rights reserved.
http://dx.doi.org/10.1016/j.ijrmms.2012.12.011

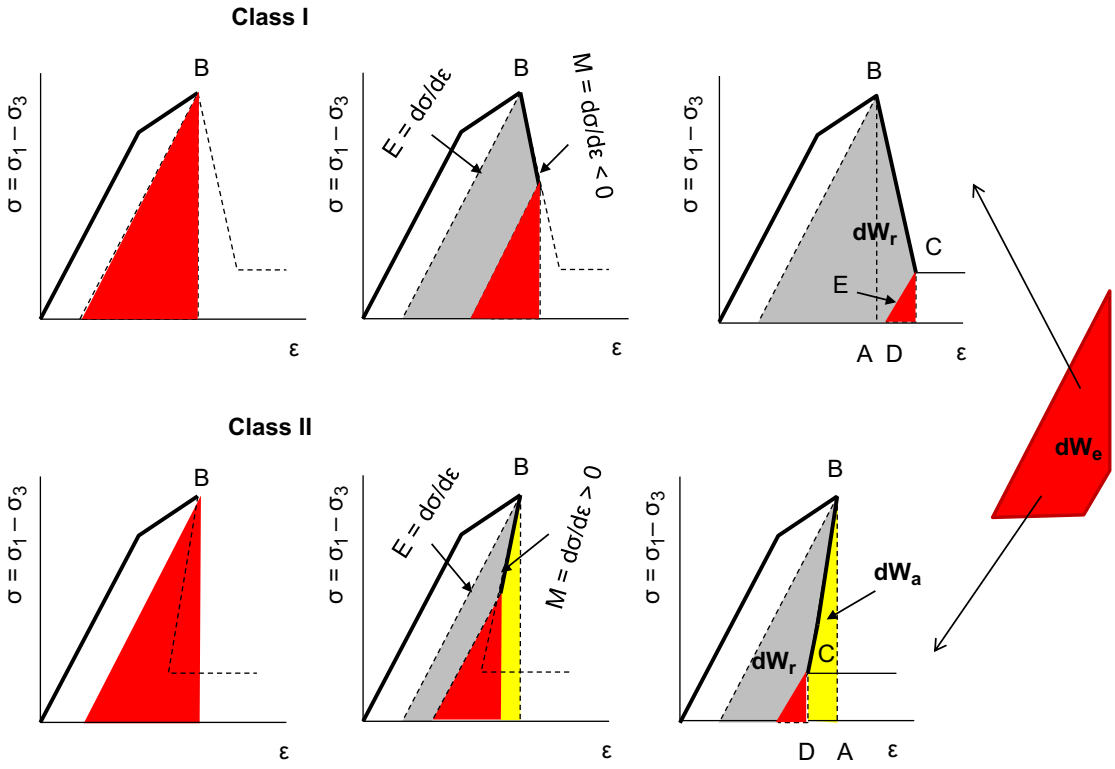

Fig. 1. Illustration of the post-peak energy balance for rocks of Class I and Class II behaviour. (For interpretation of the references to colour in this figure caption, the reader is referred to the web version of this article.)

the complete stress–strain diagrams. It is known that rock behaviour in the post-peak region can be characterised by negative or positive post-peak modulus $M=d\sigma/d\varepsilon$, where σ is the differential stress $(\sigma_1-\sigma_3)$ and ε is the axial strain. In accordance with classification proposed in [20] $M<0$ corresponds to Class I behaviour while $M>0$ corresponds to Class II behaviour.

The complete stress–strain curves in Fig. 1 illustrate Class I and Class II behaviour in the post-peak region. The graphs show the energy balance at three stages of deformation: at the peak stress (point B), at an intermediate post-peak stage, and at the complete failure (point C). Areas of the red triangles here correspond to elastic energy stored within the specimen at the three mentioned stages of deformation. The grey areas represent the post-peak rupture energy.

The graphs illustrate the dynamics of transforming the elastic energy accumulated within the specimen material at peak stress, into post-peak rupture energy. The red areas (elastic energy) are partly replaced in the graphs by the grey areas (rupture energy). The elastic energy represents the source of the post-peak failure process and provides the physical basis for the post-peak failure regime. For Class II, the fracture development occurs entirely due to the elastic energy available from the material. The failure process has a self-sustaining character, with the release of excess energy, corresponding to the yellow area (ABCD). The released energy can be transformed into the failure process dynamics, particularly associated with fragmentation, flawing fragments, seismicity, heat, etc. For Class I, the amount of elastic energy available from the material is not sufficient to produce failure, and some additional amounts of energy (the grey area ABCD) are required to support this process.

Brittleness indices based on the ratio between the elastic energy withdrawn from the material during the failure process and the post-peak rupture energy (or released energy) can be used to characterise the capability of the rock for self-sustaining failure due to the elastic energy available from the material. Such brittleness indices actually characterise the degree of intrinsic instability of the material at failure. The graphs in Fig. 1 can therefore be used to determine brittleness from energy parameters. For simplified estimation of the elastic energy dW_e withdrawn from the material specimen during the post-peak failure process between points B and C (red area on the right), it is assumed that the elastic modulus $E=d\sigma/d\varepsilon$ is the same at both points. It should be noted that the modulus E represents the unloading elastic modulus

$$dW_e=\frac{\sigma_B^2-\sigma_C^2}{2E} \tag{1}$$

The graphs show that the post-peak rupture energy dW_r is determined by the amount of withdrawn elastic energy dW_e plus the additional energy corresponding to the grey area ABCD in the case of Class I behaviour, or minus the released energy corresponding to the yellow area ABCD in the case of Class II behaviour. The additional (or released) energy is described by

$$dW_a=\frac{\sigma_B^2-\sigma_C^2}{2M} \tag{2}$$

here the post-peak modulus M is negative for Class I and positive for Class II behaviour.

The post-peak rupture energy dW_r is described by

$$dW_r=dW_e-dW_a=\frac{(\sigma_B^2-\sigma_C^2)(M-E)}{2EM} \tag{3}$$

This equation takes into account the sign of post-peak modulus M for Class I and Class II behaviour. The brittleness index K_1 below is determined by the ratio between the post-peak rupture energy and the withdrawn elastic energy [1–3]

$$K_1=\frac{dW_r}{dW_e}=\frac{M-E}{M} \tag{4}$$

The brittleness index K_2 represents the ratio between the released and the withdrawn elastic energy [1–3]

$$K_2 = \frac{dW_\alpha}{dW_e} = \frac{E}{M} \tag{5}$$

It is known that the unloading elastic modulus E and the post-peak modulus M can vary significantly with the fracture development. However, two infinitely near points located on a post-peak curve (for example points B and C in Fig. 2) can be characterised by the same value of E. The corresponding modulus M is determined on the basis of a tangent line. Increments of withdrawn elastic energy dW_e (red area), post-peak rupture energy dW_r (grey area), and released energy dW_a (yellow area) associated with fracture development between the neighbouring points B and C are described precisely by Eqs. (1)–(3). Using Eqs. (4) and (5), brittleness indices K_1 and K_2 can be determined for any stage of the post-peak process.

Brittleness indices K_1 and K_2 allow designing a continuous, monotonic and unambiguous scale of brittleness. Fig. 3 shows scales of rock brittleness indices K_1 and K_2 with brittleness increasing from left to right [1–3]. The complete curves (differential stress σ vs. axial strain ε_1) illustrate how the different curve shapes describe a variation in brittleness. It is assumed, for simplicity, that the pre-peak parts of the curves are the same. Areas defined by the large red triangles correspond to elastic energy W_e stored within the rock material at peak stress, while the smaller red dotted triangles on the right side of the curves represent the unconsumed portion of the stored elastic energy, within the material, after failure. The post-peak parts of the curves characterised by the post-peak modulus M and indicated by blue dotted lines are different for each curve. The grey areas represent the post-peak rupture energy dW_r associated with strength degradation on the value $d\sigma$ at failure from the peak stress to the residual strength (horizontal part of the post-peak curves).

Fig. 3 shows variation in brittleness from absolute brittleness to ductility. The absolute brittleness has the following characteristics and parameters: (a) the post-peak modulus is the same as the elastic modulus $M=E$; (b) there is no portion of the stored energy transformed into post-peak rupture energy $dW_r=0$; (c) the withdrawn elastic energy is entirely transformed into released energy $dW_e=dW_a$; (d) $K_1=0$, and (e) $K_2=1$.

Within the range of brittleness indices $1>K_1>0$ and $0<K_2<1$ (pink area) the elastic energy dW_e withdrawn from the specimen material during stress degradation on the value $d\sigma$ exceeds the corresponding rupture energy dW_r, leading to self-sustaining failure (Class II behaviour). The self-sustaining failure

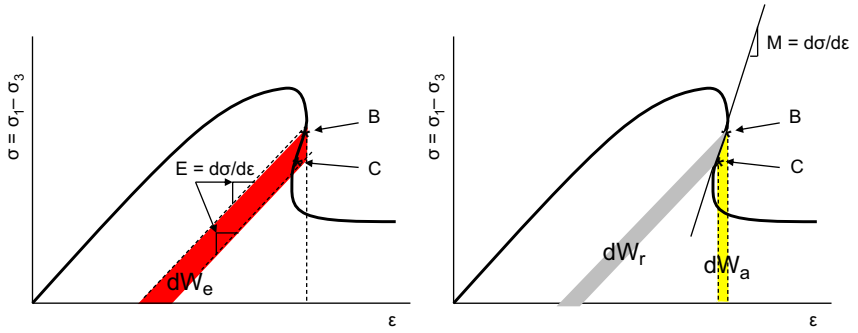

Fig. 2. Illustration of local brittleness estimation by brittleness indices K_1 and K_2 at failure between points B and C. Here red, grey and yellow areas represent correspondingly the withdrawn elastic energy dW_e, rupture energy dW_r and released energy W_a. (For interpretation of the references to colour in this figure caption, the reader is referred to the web version of this article.)

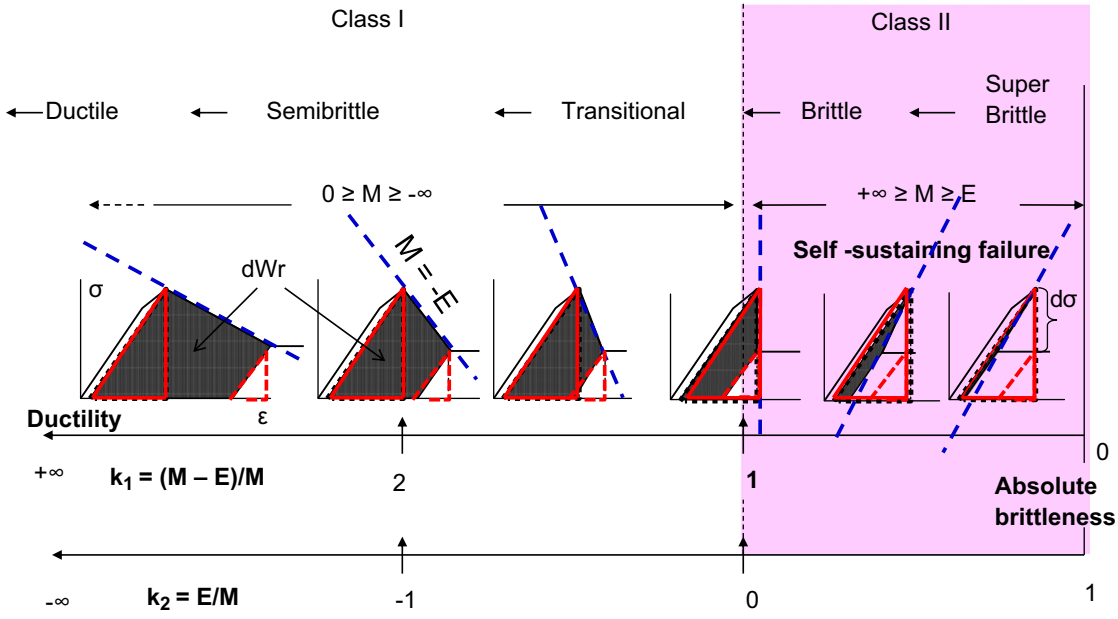

Fig. 3. Scale of brittleness indices K_1 and K_2 with characteristic shapes of complete stress–strain curves (modified from [1–3]). (For interpretation of the references to colour in this figure caption, the reader is referred to the web version of this article.)

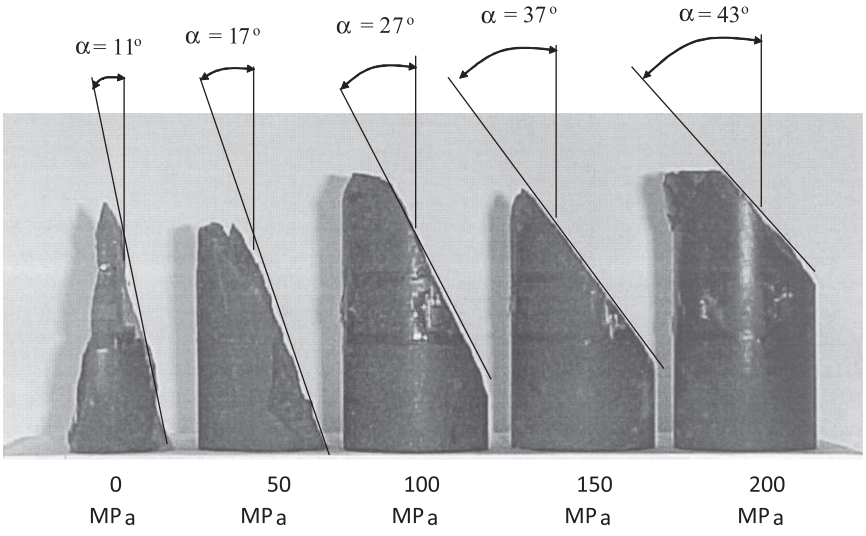

Fig. 4. Dolerite specimens tested at different levels of confining pressure.

normally has a spontaneous character even for a hypothetically perfectly stiff testing machine. The greater the difference between dW_e and dW_r the closer the material behaviour is to absolute brittleness and the more violent the self-sustaining failure. It should be noted that the use of very stiff and servo-controlled loading machines allows, in many cases, to produce a controllable failure for rocks characterised by the positive post-peak modulus M, due to the extraction of the excess of elastic energy from the material body.

For the range of brittleness indices $+\infty > K_1 > 1$ and $-\infty < K_2 < 0$ the rupture development is not self-sustaining (Class I behaviour). Variation in failure regimes corresponding to an increase in the rock brittleness is indicated in the upper part of Fig. 3. These regimes are: ductile, semi-brittle, transitional, brittle and superbrittle. The characteristic features of the superbrittle regime are discussed in [1–3].

3. Features of post-peak properties determination

3.1. Specimen size and strain measurement

It is self-evident that for comparison of material properties (including brittleness), tested specimens should have similar geometry and size. The world testing experience shows that the most suitable shape of specimens for testing at confined compression is cylindrical with a ratio between length and diameter of 2–3. General diameters of cylindrical specimens tested at confined compression are between 20 and 60 mm. Such variation in size is quite small to cause appreciable size effect. At the same time, some methods used for the determination of stress–strain curves can lead to very serious errors in defining post-peak properties and rock brittleness. This question is discussed below.

It is known that the failure mode at confined compression is shear (see Fig. 4). In this situation, elastic energy accumulated within the relatively evenly deformed material at the peak stress is used for localised shear rupture development in the post-peak region. Hard rock specimens can fail with the formation of very thin shear ruptures. The fault thickness measured for the dolerite specimen tested at $\sigma_3 = 150$ MPa was about 0.1 mm. The irreversible deformation is concentrated within this thin zone while the rest specimen body is subjected to elastic unloading in the post-peak region. Variation in confining pressure changes the angle α of shear rupture orientation relative to the specimen axis (see Fig. 4). These facts (failure localisation at a specific angle α) should be taken into account for the correct determination of post-peak properties, energy balance and brittleness indices.

Fig. 5a shows a specimen at three stages of deformation: I—before loading; II–at the peak stress with elastic energy (red) stored uniformly within the specimen body; and III—after failure (completely unloaded). The amount of elastic energy stored within the specimen at the peak stress is proportional to the specimen length. At the same time, the post-peak rupture energy is the same for specimens of different length. Depending on the specimen length, we can have very different situations and very different post-peak curves. Fig. 5a shows a situation when the elastic energy (associated with elastic deformation Δ_e) is greater than the post-peak rupture energy (associated with irreversible deformation Δ_r). To prevent instability during the rupture development, the excess of elastic energy must be opportunely extracted from the specimen by the reverse deformation on the total value $\Delta_a = \Delta_e - \Delta_r$. In this situation, we have Class II behaviour. However, for a shorter specimen of the same rock, the amount of elastic energy stored at the peak stress is smaller and if $\Delta_r > \Delta_e$ the failur$_e$ process can correspond to Class I behaviour.

The position of axial gauges on the specimen is also very important. Fig. 5a-I shows symbolically four gauges fixed to different pin-points on the specimen surface. The future shear rupture shown by the dotted line is located between the pin-points of gauges 1 (length ℓ_{g1}), 2 (length ℓ_{g2}) and 3 (length ℓ_{g3}). However, gauge 4 (length ℓ_{g4}) is fixed to the solid part of the specimen. It is known that shear rupture in hard rocks develop mainly after the peak stress and propagates along its own plane due to creation of tensile cracks and blocks (slabs) between them forming the universal 'domino' structure of shear ruptures [1–3,21–27]. This structure is shown symbolically in Fig. 5a-III. Displacement along the fault during the failure process is accompanied by rotation (or collapse) of these blocks which provide approximately the same displacement Δ_r in any zone of the fault.

In the post-peak region, each of the gauges 1, 2 and 3 measures relative displacement $d\Delta$ of two pin-points fixed to the specimen surfaces. The measured displacement is determined by two types of deformation taking place between the pin-points: (a) elastic deformation $d\Delta_e$ associated with uniform elastic unloading of solid material located between the pin-points due to the strength degradation at shear rupture development. It should be noted that the elastic unloading can be provided by direct elastic deformation associated with shear along the fault and also by reverse deformation (in the case of Class II behaviour). (b) Localised irreversible displacement $d\Delta_r$ associated with shear

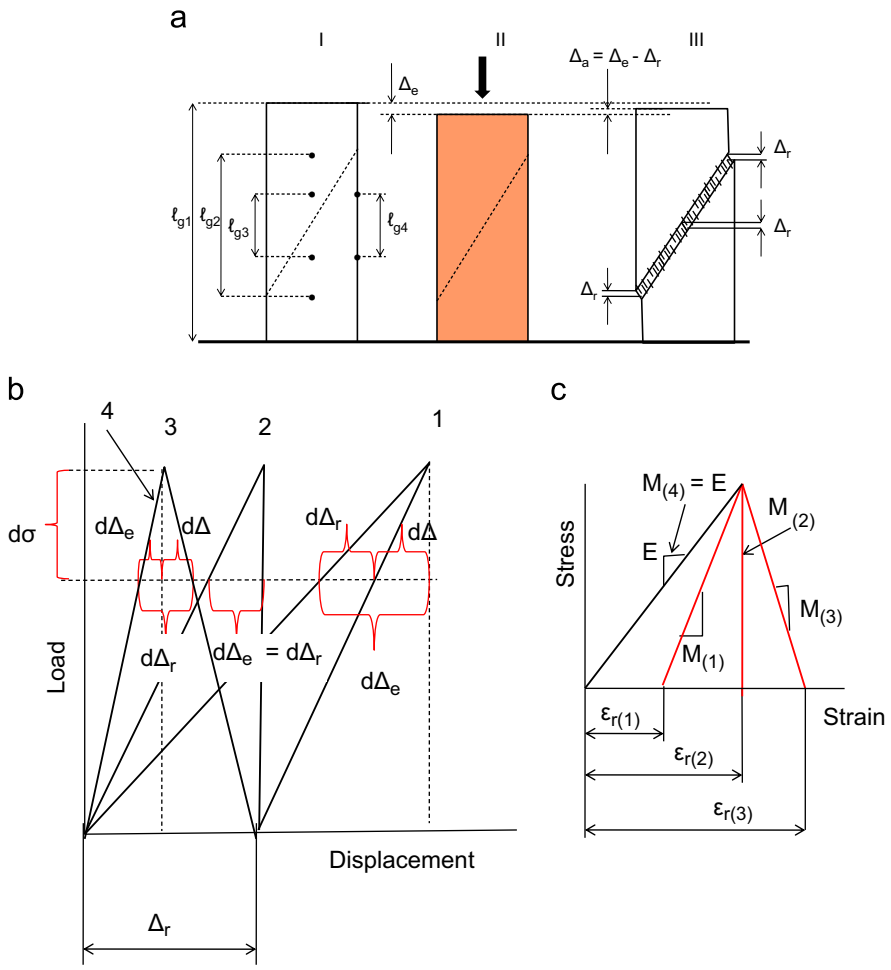

Fig. 5. (a) Schema of a specimen equipped with different axial gauges (1–4) at three stages of loading; generic (b) load–displacement and (c) stress–strain curves plotted for gauges 1–4.

along the fault:

$$d\Delta = d\Delta_r - d\Delta_e \tag{6}$$

Due to the fact that the value of $d\Delta_r$ is the same for all gauges but the value of $d\Delta_e$ is different, depending on the gauge length, load–displacement and stress–strain curves plotted on the basis of data recorded by gauges 1, 2 and 3 are very different. Gauge 4 measures just elastic unloading.

Fig. 5b illustrates graphically the fundamental difference in the shape of load–displacement curves plotted on the basis of data recorded by gauges 1–4. For simplicity, the pre-peak curves reflect elastic deformation only. The term $d\Delta$ here is the value of post-peak deformation recorded by the gauges. At stress degradation $d\sigma$ in the post-peak region, the value $d\Delta$ for the longest gauge 1 is negative, representing the reverse displacement (Class II behaviour), while for the shortest gauge 3 the value $d\Delta$ is positive (Class I behaviour). For gauge 2 we have $d\Delta = 0$. Gauge 4 indicates elastic unloading. The value of rupture energy (associated with $d\Delta_r$) recorded by gauges 1, 2 and 3 is the same. At the complete failure, the rupture energy corresponds to areas of triangles with the base Δ_r.

Corresponding stress-strain curves are shown in Fig. 5c. Before the peak stress is reached, all stress–strain curves coincide independently on the gauge length due to uniform elastic deformation of the specimen body. The localised failure in the post-peak region makes values of irreversible strain $\varepsilon_r = \Delta_r/\ell_g$ and post-peak modulus M very different for different gauges. Gauge 3 indicates Class I, while gauge 1—Class II behaviour; gauge 2 shows intermediate behaviour; gauge 4 shows elastic unloading in the post-peak region. In fact, post-peak characteristics obtained for the same specimen by different gauge lengths are fundamentally different. Brittleness indices calculated on the basis of these curves will show also incomparably different results. The question is: how can we make results recorded by different gauges for the same and also for different specimens comparable?

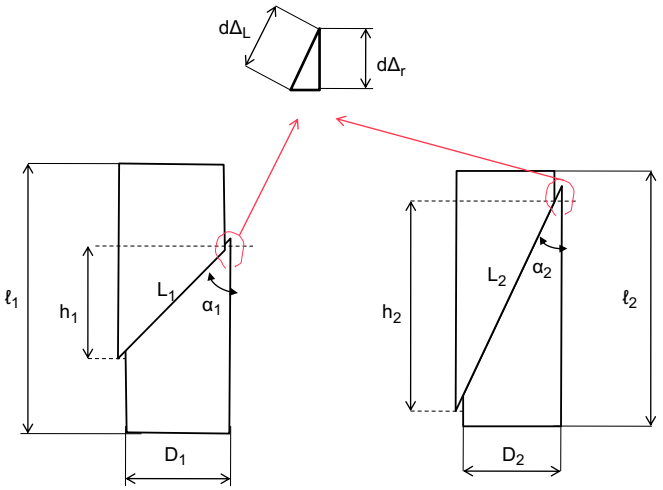

Fig. 6. Schema illustrating the principle of axial strain calculation in the post-peak region.

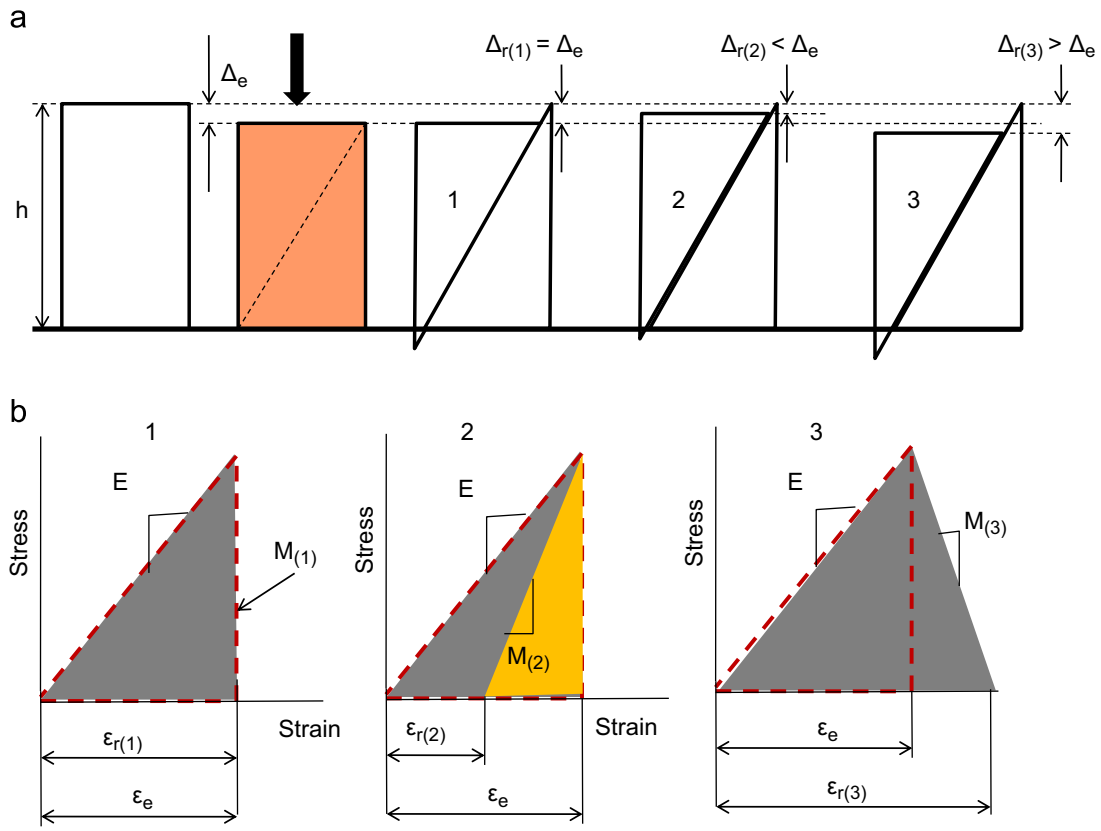

Fig. 7. (a) Features of axial deformation of zone h before and after peak stress and (b) corresponding stress–strain curves for three materials—1, 2, and 3.

Fig. 6 shows two specimens of different diameters and length. Angle α of shear plane orientation relative to the specimen axis is also different. Irreversible strain ε_r associated with displacement along the shear plane can be calculated as follows:

$$d\varepsilon_r = d\Delta_L/L = d\Delta_r/h = d\Delta_r tg\alpha/D \quad (7)$$

where L is the length of shear plane; $d\Delta_L$ is the irreversible displacement along the shear plane; $d\Delta_r$ is the corresponding axial displacement; h is the length of the specimen fragment involving the shear plane; and D is the specimen diameter.

In principle, values of $d\Delta_r$ or (Δ_r) can be obtained from load–displacement curves (similar to that shown in Fig. 5b) plotted for both long and short axial gauges specially oriented against the fault (gauges 1–3 in Fig. 5a). However, because the spatial orientation of shear plane is unknown before the test, it is a better option to use long gauges with the length $\ell_g > h$.

Stress–strain curves plotted in accordance with Eq. (7) will unambiguously characterise post-peak properties of the same specimen independently on the specimen and gauge length. This allows comparing brittleness estimated on the basis of post-peak energy balance for the same rock tested at different testing conditions or brittleness of different rocks. Brittleness indices K_1 and K_2 calculated on the basis of these curves will reflect the energy balance between the localised rupture energy and elastic energy accumulated within the specimen fragment of the length h. Fig. 7a and b illustrates features of axial deformation of zone h and corresponding stress–strain curves for three materials (1, 2, and 3) characterised by the same strength, elastic modulus and, consequently, elastic energy at the peak stress, but different post-peak rupture energy. Experimental stress–strain curves presented further are plotted using the approach discussed in this paragraph.

3.2. Strain rate and control of post-peak stability

It is known that strain rate affects significantly the shape of stress–strain curves. When studying the effect of strain rate on rock properties, a constant strain rate during the whole test before and after peak stress should be maintained [28,29]. This testing condition can be provided for Class I behaviour only because stress–strain curves monotonically increase in strain. For Class II behaviour, because of the reverse deformation of the sample in the post-peak region, it is principally impossible to maintain a constant strain rate during the test and correctly record the post-peak part of load–displacement curves in dynamics. The ISRM proposed a suggested method (SM) advising on the complete load–displacement behaviour of rock specimens that allows comparison of data between materials, laboratories and researchers [30]. The SM suggests axial strain rate of 10^{-6} strain/s.

It is known also that axial strain control is impossible for Class II behaviour because the curve does not monotonically increase in strain. Circumferential or diametrical strain control is suggested by ISRM SM because this measurement does monotonically increase even if the axial displacement does not. The suggested circumferential or diametrical strain rate is 10^{-4} strain/s. In accordance with ISRM SM stiffness of loading frame and loop-closure rates of control system should be respectively no less that 5 MN/mm and 1 kHz.

Experimental results discussed below were obtained on a stiff servo-controlled testing machine with stiffness 40 MN/mm, load capacity 2000 kN, confining pressure up to 200 MPa [31]. Axial strain control was used for Class I behaviour and diametrical strain control for Class II behaviour. Strain rate was provided in accordance with ISRM SM. Dimensions of specimens were: diameter 35 mm and length 80 mm.

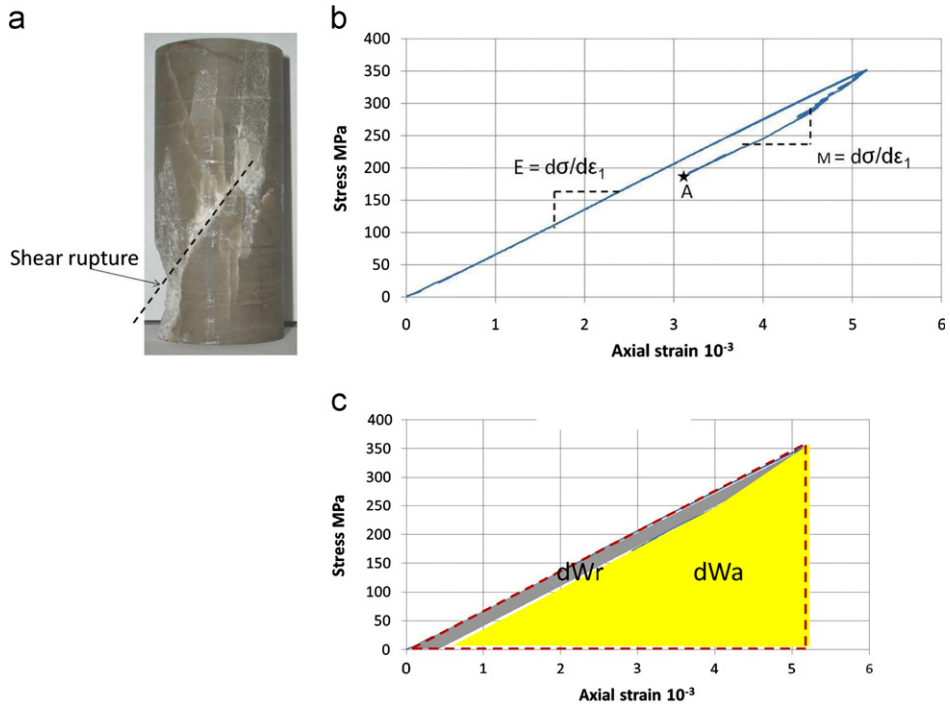

Fig. 8. (a) A quartzite specimen after testing at uniaxial compression and corresponding, (b) stress–strain curve and (c) post-peak energy balance.

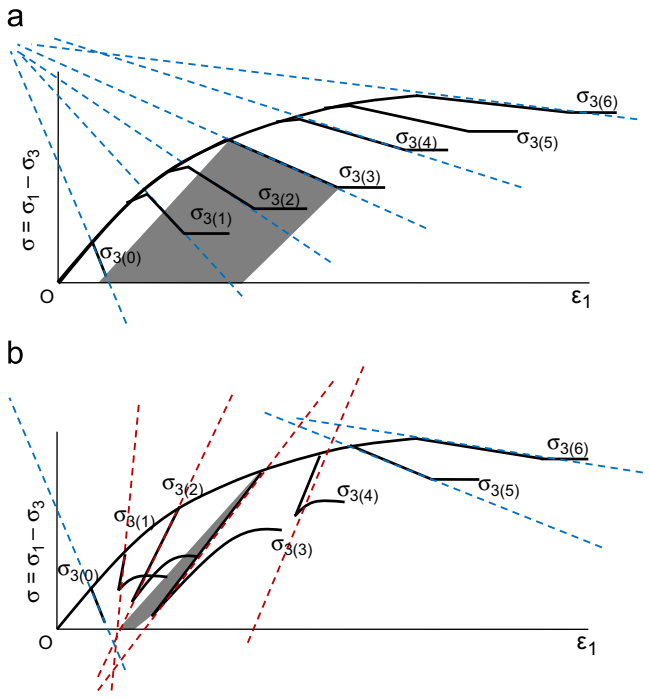

Fig. 9. Two types of rock behaviour in the post-peak region under the effect of confining pressure σ_3. (For interpretation of the references to colour in this figure caption, the reader is referred to the web version of this article.)

Fig. 8 illustrates testing capability of the machine. A very brittle quartzite specimen (Fig. 8a) was tested at uniaxial compression. The corresponding stress–strain curve is shown in Fig. 8b. The post-peak stage is associated with shear rupture development. The testing procedure was stopped at point A before the complete failure, after which the specimen was unloaded. The specimen shows Class II behaviour with post-peak modulus M close to elastic modulus E. Fig. 8c indicates rupture energy dW_r absorbed by the failure process before the point A and corresponding portion of extracted energy dW_a. The failure process was stable due to servo-controlling.

4. Brittleness variation due to confining pressure

For all rocks, the pre-peak ductility increases with rising confining pressure σ_3. Beyond the peak stress, the situation is different: two types of rock behaviour in the post-peak region under the effect of confining pressure can be distinguished. The first one is associated with increasing post-peak ductility with rising confining pressure σ_3. This conventional type of rock behaviour illustrated in Fig. 9a shows a set of generic stress–strain curves for different σ_3. To show clearly the character of variation of the post-peak curves indicating the increase in post-peak ductility with rising σ_3 they are represented by blue (Class I) dotted lines. The shaded area under the curve $\sigma_{3(3)}$ corresponds to post-peak rupture energy under this testing condition.

Unlike the conventional type of rock behaviour, recently published papers [1–3] showed that increasing σ_3 can lead to contradictory (unconventional) rock behaviour within different ranges of σ_3. In fact, rock behaviour can be changed from Class I to Class II and then to Class I again as shown in Fig. 9b. Post-peak curves corresponding to Class II are represented by red dotted lines. Such variation of post-peak curves with rising σ_3 indicates the following variation in brittleness: initially increasing, reaching a maximum and then ultimately decreasing. The shaded area under the curve $\sigma_{3(3)}$ representing the post-peak rupture energy under this testing condition can be very small.

Experimental curves illustrating the two types of rock behaviour under confining pressure discussed above are shown in Fig. 10a (sandstone), b (quartzite), and c (dolerite) [1–3]. Fig. 11 shows the variation of brittleness index K_1 and K_2 for these rocks and also for Westerly granite [32]. It demonstrates different responses to rising confining pressure σ_3. The self-sustaining failure regime corresponds to $1 > K_1 > 0$ and $0 < K_2 < 1$ (pink area).

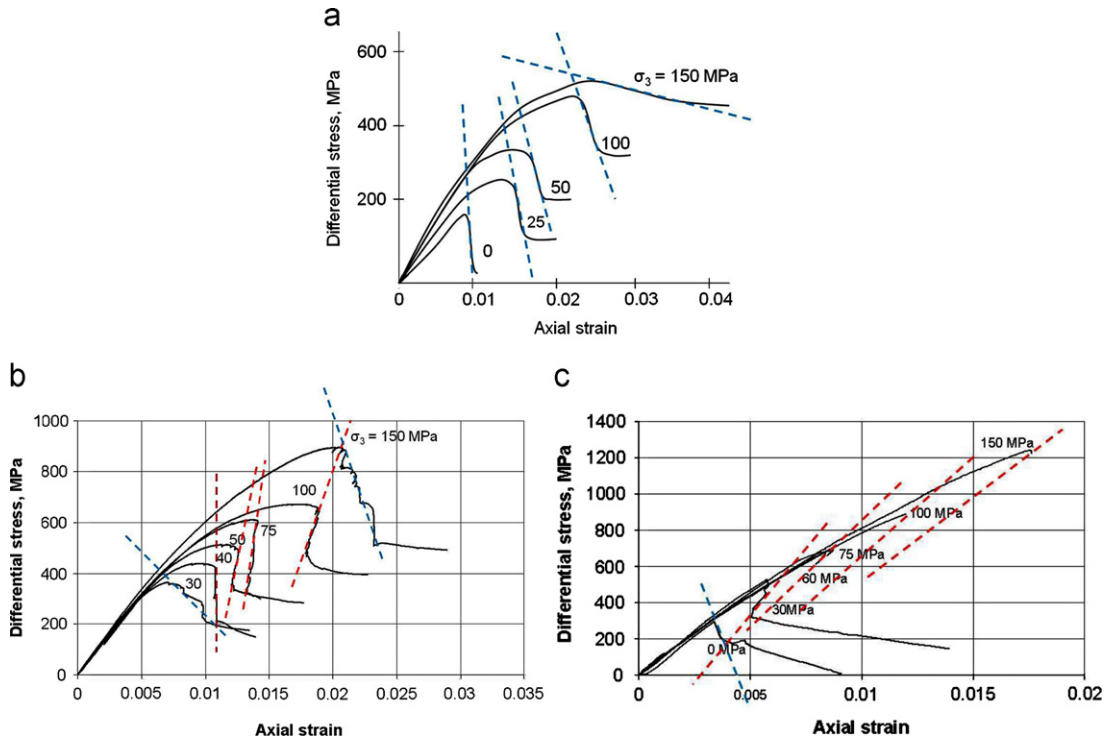

Fig. 10. Stress–strain curves for (a) sandstone, (b) quartzite, and (c) dolerite obtained at different σ_3 (modified from [1–3]).

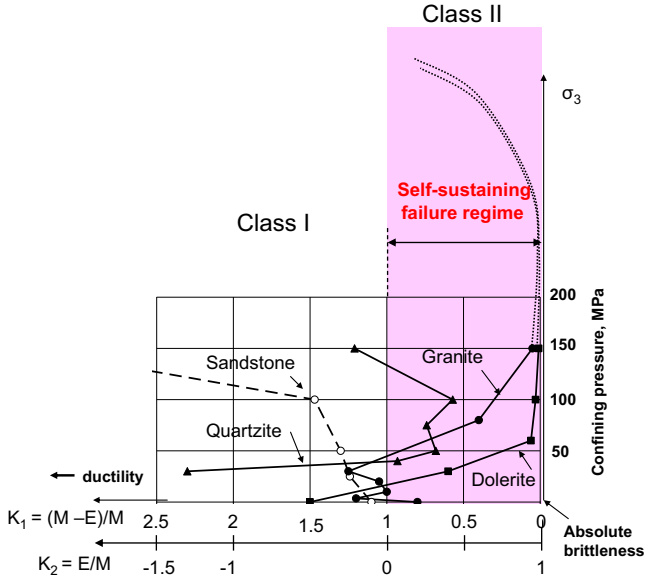

Fig. 11. Variation of brittleness indices K_1 and K_2 versus confining pressure σ_3 for rocks of different hardnesses (modified from [1–3]). (For interpretation of the references to colour in this figure caption, the reader is referred to the web version of this article.)

The sandstone curve indicates that an increase in confinement σ_3 makes the rock less brittle. This behaviour is typical for softer rocks. For the quartzite, an increase in confinement σ_3 within the range of 30–100 MPa makes the material more brittle. At greater confinement, the brittleness decreases. For the granite, an increase in σ_3 within the range of 0–30 MPa makes it less brittle. When $\sigma_3 > 30$ MPa, the brittleness increases dramatically. The dolerite curve shows also very severe rock embrittlement. At $\sigma_3 = 75$ MPa, according to the brittleness index K_1, the dolerite became 250 times more brittle when compared to uniaxial compression ($K_{1(0)} = 1.5$; $K_{1(75)} = 0.006$). At $\sigma_3 = 100$ and 150 MPa, the brittleness increased significantly, further approaching absolute brittleness. The dotted lines indicate the expected brittleness variation for granite and dolerite at greater values of σ_3: the brittleness continues to increase until it reaches a maximum at some level of σ_3 and then decreases, as all rocks become ductile at very high σ_3. It is estimated in [1,3] that the maximum brittleness for granite is reached at $\sigma_3 \approx 300$ MPa. For rocks that are as hard as quartzite, the mode of brittleness variation is similar, but the maximum brittleness is lower and the range of confining pressure where embrittlement takes place is smaller.

5. Failure mechanisms providing high (Class I) and low (Class II) rupture energy at shear

Shear rupture never develops instantly but it propagates through the material in time. Fig. 12a shows four stages of shear rupture development in a specimen when subjected to triaxial compression. A load cell and an axial gauge mounted on the specimen as shown in Fig. 12a-i can measure the average load-bearing capacity and the strain of the specimen during the failure process. The real shear resistance and displacement along the future failure plane are very non-uniform. Three specific zones can be distinguished (see Fig. 12a-ii): (1) the process zone (or rupture head) where the failure process is in progress; (2) the core frictional zone located behind the head where the full friction is mobilised, and (3) the intact zone in front of the head where the resistance is determined by the cohesive strength. With fracture propagation, the cohesive strength of decreasing zone (3) is substituted by the frictional resistance of increasing zone (2). This process is accompanied by the decrease in bearing capacity of the specimen from the cohesive strength to the frictional (residual) strength. The fracture mechanism operating within the process zone (1) plays the key role in the character of transformation from the cohesive to frictional strength.

It is known that a shear rupture can propagate in its own plane due to the creation of short tensile cracks in front of the rupture

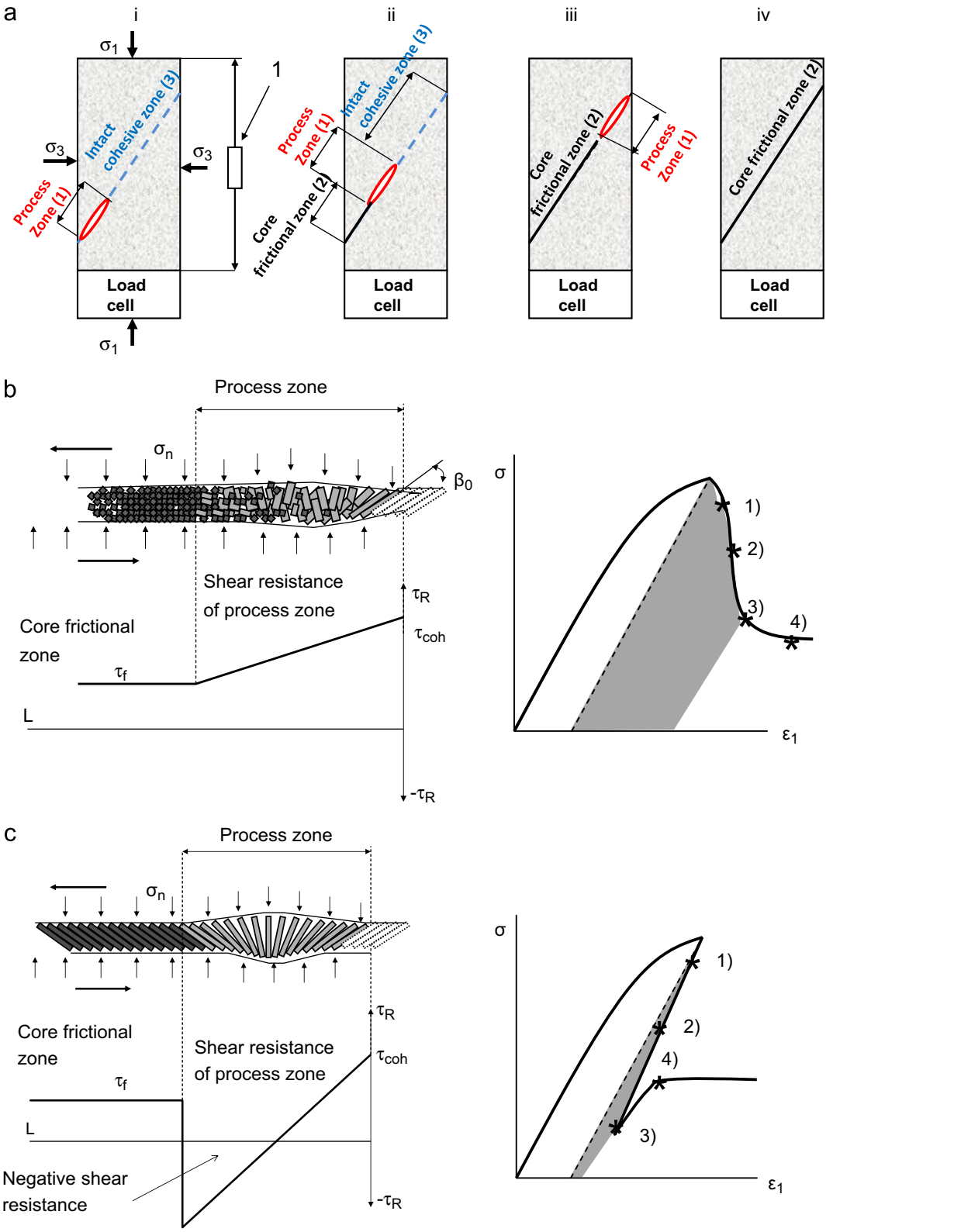

Fig. 12. (a) Four stages of shear rupture development in a specimen at triaxial compression, (b) frictional and (c) frictionless concepts of shear fracture development.

tips [21–23]. This forms the universal structure of shear ruptures represented by an echelon of blocks (or slabs) separated by tensile cracks—known as a 'domino' structure [21–25] or Ortlepp shears [26,27]. The initial angle β_0 of the tensile crack and block inclination to the shear rupture plane is about 30–40° [33]. Shear displacement along the fault causes rotation of the blocks of the 'domino' structure between the rupture surfaces [22–25].

Fig. 12b illustrates the essence of the shear rupture mechanism providing large rupture energy. Blocks located in the front part of the process zone create significant resistance to shear; however, they collapse with rotation providing gradual transformation of shear resistance within the process zone from cohesive to frictional levels. A graph under the shear rupture in Fig. 12b shows the shear resistance variation along the process zone.

The crushing and comminution of blocks within the process zone can absorb large amounts of energy. This is expected since the development of shear fractures requires displacement to occur along the total fault. This form of rupture development is classified as a crack-like mode. Such rupture mechanism normally produces a Class I material behaviour in the post-peak region. Four points on the stress–strain curve on the right correspond to the four stages of deformation shown in Fig. 12a. The grey area corresponds to post-peak rupture energy at the stage 4.

Fig. 12c illustrates a model where rotating blocks can withstand the rotation without collapse behaving as hinges (see details in [1–3]). Due to consecutive formation and rotation of the blocks, these should form a fan structure within the rupture head. A remarkable feature of the rotating blocks (hinges) in the second half of the fan structure (where $\beta > 90^{\circ}$) is the creation of active forces under the effect of normal stress applied. A graph under the shear rupture in Fig. 12c shows the shear resistance variation along the fault head. The bottom part of the graph represents active forces (negative resistance) acting in the second half of the head and assisting the fault displacement. In the core zone represented by blocks that have completed their rotation, the normal residual friction is restored.

The fan structure represents a self-equilibrating mechanism and can move spontaneously as a wave with very small shear resistance. In the idealised fan-head model the resistance to rupture propagation is determined only by the tensile strength of the material associated with consecutive formation of blocks in front of the propagating rupture. It is important that the fan head can propagate independently of the core zone, which can remain immobile due to high frictional resistance. Hence, this mechanism creates conditions for a pulse-like mode of fracture propagation. In this situation, the rupture energy is determined by shear resistance of the fan-head only. The fan-head rupture mechanism represents the most energy efficient shear rupture mechanism.

This mechanism is responsible for Class II behaviour with extremely small rupture energy (grey area) approaching the absolute brittleness. The stress–strain curve in Fig. 12c shows that at stage 3 of the fracture propagation the bearing capacity of the specimen can be less than that at stage 4. This is because the shear resistance of the process zone can be close to zero, decreasing the bearing capacity of the specimen. The longer the process zone (1), the smaller the shear resistance at stage 3 of the rupture propagation. The fully frictional resistance is mobilised at stage 4 after the head has completely propagated through the specimen. The examples discussed show that shear rupture mechanisms involving the book-shelf structure can be responsible for the delay in friction mobilisation at failure observed in experiments.

Natural shear fractures can be at different stages of their development. Their shear resistance and brittleness at the post-peak failure stage can correspond symbolically to different points on the stress–strain curves shown in Fig. 12b and c. The brittleness (degree of instability) and energy release during the rupture development depends on the failure stage and the rupture mechanism. The discussed brittleness indices K_1 and K_2 can be used for the characterisation of stability conditions at any stage of failure.

6. Analysis of other brittleness indices

It was shown above that the criteria K_1 and K_2 relying upon post-peak energy balance allow for the representation of two classes of rock behaviour (Class I to Class II) in the form of continuous, monotonic and unambiguous scale of brittleness. They are based on sound physics principles reflecting the degree of post-peak instability. In this section we will analyse whether other existing criteria can provide an unambiguous characterisation of rock brittleness representing post-peak instability.

Brittleness indices similar to K_1 and K_2 were proposed in [4–8]

$$k_3 = \frac{M}{E+M} \quad [4,5] \tag{8}$$

$$k_4 = \frac{M}{E} \quad [5-8] \tag{9}$$

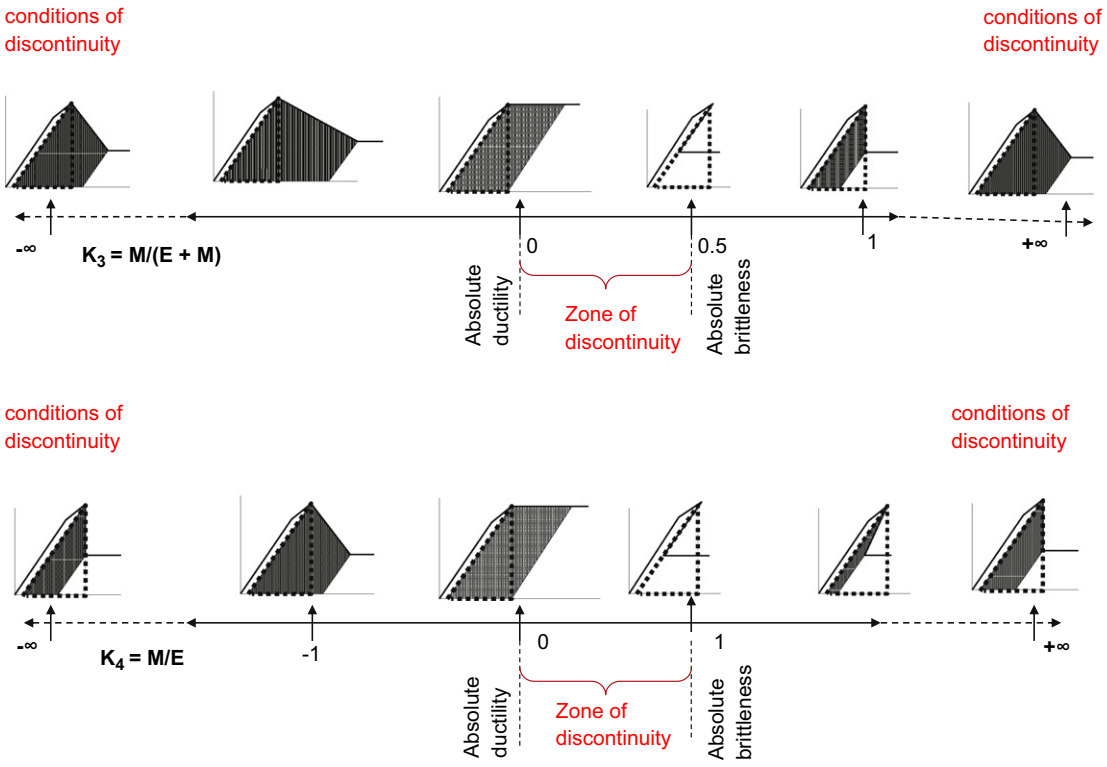

Fig. 13. Scales of brittleness indices k_3 and k_4 with characteristic shapes of complete stress–strain curves.

The brittleness indices k_3 and k_4 include some uncertainties which can lead to conflicting results for estimating the brittleness at different loading conditions. Additionally, these indices do not allow the creation of continuous and unambiguous scale of brittleness similar to the one presented in Figs. 3 and 11. Two scales of brittleness for k_3 and k_4 are shown in Fig. 13. Both scales of brittleness are stretched between $-\infty$ and $+\infty$, and the extreme points of each scale ($-\infty$ and $+\infty$) are characterised by the same shape of stress-strain curves. Another zone of discontinuity is located in a central part of the scales between conditions of the absolute brittleness and absolute ductility. Hence, the brittleness indices k_3 and k_4 are not ideal for brittleness characterisation of different rocks or the same rock at different levels of confining pressure.

Brittleness indices representing ratios of different combinations between pre-peak and post-peak strain (k_5 and k_6, Eqs. (10) and (11)) were discussed in [9–11]. Note that ε_e is the elastic strain, ε_p is the post-peak strain and ε_{tp} is the total irreversible post-peak strain

$$k_5 = \frac{\varepsilon_p}{\varepsilon_e} \tag{10}$$

$$k_6 = \frac{\varepsilon_{tp}}{\varepsilon_e} \tag{11}$$

These strain-based indices also give ambiguous results when used to characterise brittleness. For example, three stress–stain curves in Fig. 14 have the same elastic modulus E. At some stages of post-peak deformation, they have very different post-peak modulus M and post-peak rupture energy (shaded areas), which suggests very different degrees of brittleness. However, brittleness indices k_5 and k_6 based on ratios between values of elastic and post-peak deformations determined at a stage shown in Fig. 14 have the same value for all three rocks.

Brittleness indices based on different combinations of other parameters may also give conflicting results at different loading conditions because unlike K_1 and K_2, they do not have any physical foundation. A number of examples are discussed below.

Brittleness indices (k_7, k_8, and k_9) involving pre-peak irreversible deformation ε_{ir} and pre-peak irreversible energy W_{ir} have also been proposed [12–15]:

$$k_7 = \frac{\varepsilon_e}{\varepsilon_{ir}+\varepsilon_e} \quad [12,13] \tag{12}$$

$$k_8 = \frac{W_e}{W_{ir}+W_e} \quad [13,14] \tag{13}$$

$$k_9 = \frac{W_{ir}}{W_e} \quad [13-15] \tag{14}$$

Graphs in Figs. 9 and 10 show that there is no correlation between pre-peak and post-peak parameters characterising rock brittleness. Rising confining pressure causes the increase in pre-peak ductility associated with the increase in the pre-peak irreversible deformation ε_{ir} and the corresponding pre-peak rupture energy W_{br}. However, in the post-peak region, the rock behaviour is conflicting: sandstone increases ductility, while quartzite and dolerite show very severe embrittlement. Hence, indices k_7, k_8, and k_9 are not adequate for practical application.

The determination of intrinsic material brittleness from compressive R_c and tensile R_t strengths indices (e.g. $k_{10}=R_c/R_t$ [16–18]) also gives conflicting results when samples are tested under triaxial compression. It is accepted that an increase in the ratio R/R_t indicates the increase in brittleness [16–18]. In accordance with this criterion, rising confining pressure should be followed by the increase in brittleness due to more intensive rising of R_c compared with R_t. However, the experimental results discussed above show that rising σ_3 can cause both an increase and a decrease in rock brittleness.

A determination of brittleness k_{11} from Mohr's envelope [13] implies a decrease in brittleness with rising confining pressure σ_3 and cannot reflect rock embrittlement within a certain range of high σ_3.

A special strain-dependent brittleness index k_{12} was introduced to consider the contribution of the cohesive and frictional strength components during the failure process [19]. From the physical point of view, the brittleness index k_{12} reflects the presence of both tensile and shear mechanisms in inducing microcracks. This concept, however, implies an increase in ductility with rising confining pressure. Therefore, this cannot explain the very severe embrittlement observed in hard rocks under increasing confinement (σ_3) and extremely low rupture energy at high levels of σ_3.

7. Relative rock brittleness and applications

Fig. 15a shows two generic load–displacement curves for two different rocks obtained from specimens of the same dimensions and strength. These two rocks have the same brittleness index K_1 and K_2 because they are characterised by the same ratio between the elastic and post-peak modules: $E'_1/M'_1=E'_2/M'_2$. However, the behaviour of these rocks during testing on the same loading system can be very different. The dotted lines on the graph characterise the stiffness L of the loading system. For rock number 1, $L<M'_1$ and in accordance with [34], post-peak failure should be unstable due to an excess of elastic energy available from the loading system (red area). For rock number 2, $L>M'_2$ and failure should be stable because some additional energy corresponding to the grey area is transfer from the loading system. On the basis of Eq. (15), the brittleness of these two rocks can be determined in relation to the loading system (relative brittleness). Such classification of brittleness reflects the relative brittleness of rocks

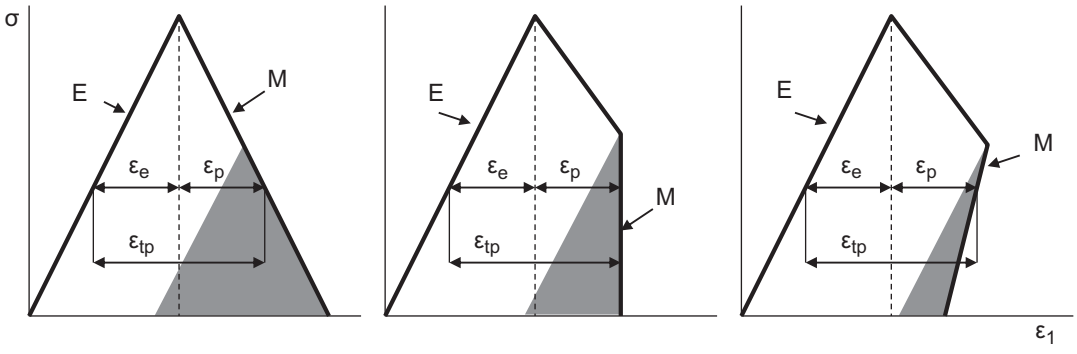

Fig. 14. Schema for estimation of rock brittleness from elastic and post-peak deformations.

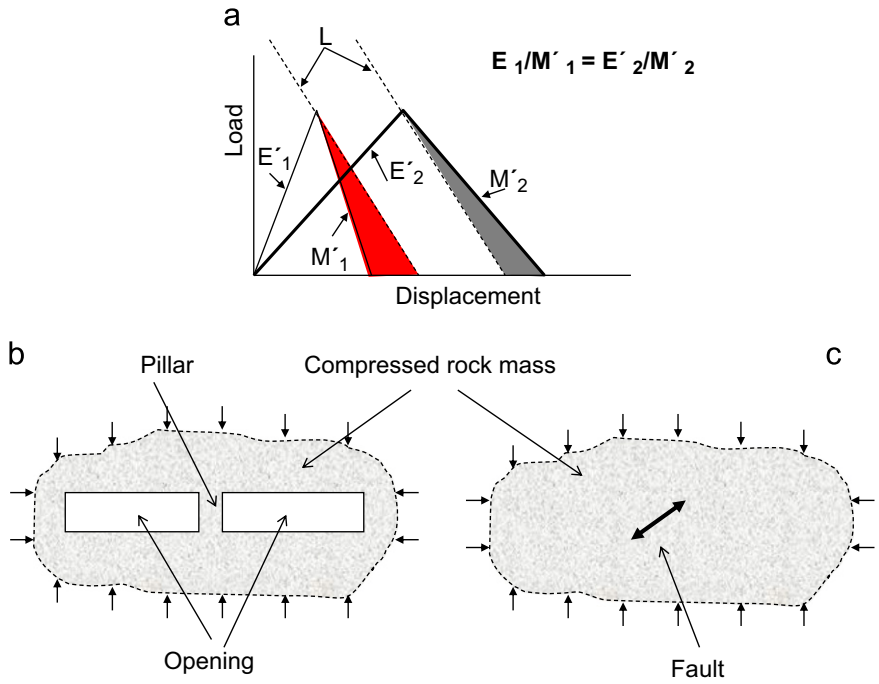

Fig. 15. (a) Load–displacement curves for two rocks having the same intrinsic and different relative brittleness; (b) rock mass involving an underground excavation with a pillar; (c) rock mass involving a shear fracture.

instead of the intrinsic material brittleness:

$$k_R = \frac{L}{M} \quad [34] \tag{15}$$

The use of intrinsic or relative brittleness for estimation of degree of instability in practice depends on loading conditions. For instance, rock mass surrounding an extended underground excavation represents a loading system with respect to pillars supporting the excavation (see Fig. 15b). In this case, the degree of instability of this construction can be characterised by index k_R representing relative brittleness. In the case of fault propagation within intact rock mass (Fig. 15c), the use of intrinsic brittleness indices K_1 and K_2 is more appropriate.

8. Conclusion

The applicability of various criteria for assessing rock brittleness under triaxial compression has been analysed. It has been shown that only two of many existing criteria can describe properly the intrinsic material brittleness within the whole range of brittleness variation from the absolute brittleness to ductility. These criteria are based upon the balance between elastic energy accumulated within the material specimen and two forms of post-peak energy associated with the failure process: the rupture energy and the excess (released) energy. The brittleness indices based on the ratio between these parameters allow for the representation of the two classes of rock behaviour (Class I and Class II) in the form of continuous, monotonic and unambiguous scale of brittleness. Other existing criteria do not provide unambiguous characterisation of rock brittleness at different loading conditions under triaxial compression. Some features of methods used for determination of post-peak properties have been discussed in this paper.

Acknowledgements

This work has been supported by the Centre for Offshore Foundation Systems (COFS) at the University of Western Australia, which was established under the Australian Research Council's Special Research Centre scheme and is now supported by the State Government of Western Australia through the Centre of Excellence in Science and Innovation program. This support is gratefully acknowledged.

References

[1] Tarasov BG. Superbrittleness of rocks at high confining pressure. In: Proceedings of the fifth international seminar on deep & high stress mining; 2010. p. 119–33.
[2] Tarasov B.G. Universal scale of brittleness for rocks failed at compression. In: Proceedings of the 13th international conference of the international association for computer methods and advances in geomechanics; 2011. p. 669–73.
[3] Tarasov BG, Randolph MF. Superbrittleness of rocks and earthquake activity. Int J Rock Mech Min Sci 2011;48:888–98.
[4] Batougina IM, Petoukhov IM, Vinokur BS, Smirnov VA, Rabota EN. Methodological instructions for rockburst prophylaxis accounting the deposit geodynamics. Leningrad: VNIMI; 1983.
[5] Stavrogin AN, Protossenia AG. Rock strength and excavation stability in great depth. Moscow: Nedra; 1985.
[6] Petoukhov IM, Linkov AM. Mechanics of rockburst and outburst. Moscow: Nedra; 1983.
[7] Manjikov BT, Mansourov VA, Pougacheva TN, Tileguenov KT. Laboratory estimation of rockbursting danger. Frounze, Ilim: SSDRRMODMA; 1983 p. 106–16.
[8] Bergman S.G.A., Still H. Rockburst problems in a 2.6 million m3 underground crude oil storage in granite. In: Proceedings of the fifth congress ISRM; 1983, D302-D309.
[9] Andreev GE. Brittle failure of rock materials. Rotterdam: Balkema; 1995.
[10] Recommendation for determining the total Mohr strength envelope and deformability for rock. Leningrad: VNIMI; 1988.
[11] He C, Okubo S, Nishimatsu Y. A study on the class II behaviour of rock. Rock Mech Rock Eng 1990;23:261–73.
[12] Coates DF. Experimental criteria for classification of rock substances. Int J Rock Mech Min Sci 1966;3:181–9.
[13] Hucka V, Das B. Brittleness determination of rocks by different methods. Int J Rock Mech Min Sci 1974;11:389–92.
[14] Baron LI, Loguntsov BM, Posin IZ. Determination of rock properties. Moscow: NTILGD; 1962.
[15] Kidybinski A. Bursting liability indices of coal. Int J Rock Mech Min Sci 1981;18:295–304.
[16] Beron AI, Vatolin ES, Koifman MI, Mohnachev MP, Chirkov SE. Rock properties under different loading regimes. Moskow: Nedra; 1983.
[17] Walsh JB, Brace WF. A fracture criterion for brittle anisotropic rock. J Gephys Res 1964;69:3449–56.

[18] Vardoulakis I. Rock bursting as a surface instability phenomenon. Int J Rock Mech Min Sci 1984;21:137–44.
[19] Hajiabdolmajid V, Kaiser P, Martin CD. Mobilised strength components in brittle failure of rock. Geotechnique 2003;53:327–36.
[20] Wawersik WR, Fairhurst C. A study of brittle rock fracture in laboratory compression experiments. Int J Rock Mech Min Sci 1970;7:561–75.
[21] Reches Z. Mechanisms of slip nucleation during earthquakes. Earth Planet Sci Lett 1999;170:475–86.
[22] Cox SJD, Scholz CH. On the formation and growth of faults: an experimental study. J Struct Geol 1988;10:413–30.
[23] Reches Z, Lockner DA. Nucleation and growth of faults in brittle rocks. J Geophys Res 1994;99(B9):18159–73.
[24] Peng S, Johnson AM. Crack growth and faulting in cylindrical specimens of Chelmsford granite. Int J Rock Mech Min Sci 1972;9:37–86.
[25] King GCP, Sammis CG. The mechanisms of finite brittle strain. Pure Appl Geophys 1992;138:611–40.
[26] Van Aswegen G. Ortlepp shears—dynamic brittle shears of South African Gold Mines. Proceedings of the first southern hemisphere international rock mechanics symposium 2008:111–9.
[27] Ortlepp WD. Rock fracture and rockbursts. Johannesburg: SAIMM; 1997.
[28] Bieniawski ZT. Time-dependent behaviour of fractured rock. Rock Mech 1970;2:123–37.
[29] Stavrogin AN, Tarasov BG. Experimental physics and mechanics of rock. Amsterdam: Balkema; 2001.
[30] Fairhurst CE, Hudson JA. Draft ISRM suggested method for the complete stress-strain curve for intact rock in uniaxial compression. Int J Rock Mech Min Sci 1999;36:279–89.
[31] Tarasov B.G., Dyskin A.V. The phenomenon of anomalous rock embrittlement. In: Proceedings of the sixth international symposium on rockburst and seismicity in mines; 2005. p. 311–7.
[32] Wawersik WR, Brace WF. Post-failure behavior of a granite and diabase. Rock Mech 1971;3:61–85.
[33] Horii H, Nemat-Nasser S. Compression-induced microcrack growth in brittle solids: axial splitting and shear failure. J Geophys Res 1985;90:3105–25.
[34] Cook NGW. The failure of rock. Int J Rock Mech Min Sci 1965;2:389–403.